

# Spatial distribution of far infrared emission in spiral galaxies I. Relation with radio continuum emission

Y.D. Mayya<sup>1,2</sup> and T.N. Rengarajan<sup>2</sup>

<sup>1</sup>*Tata Institute of Fundamental Research, Homi Bhabha Road, Mumbai 400 005, India*

<sup>2</sup>*Instituto Nacional de Astrofisica Optica y Electronica, Apdo Postal 51 y 216, 72000 Puebla, Pue., MÉXICO*  
*Electronic Mail: ydm@inaoep.mx and renga@tifrvax.tifr.res.in*

*Accepted — June 1997. To appear in Astronomical Journal, September 1997*

## ABSTRACT

We use high resolution IRAS and 20 cm radio continuum (RC) images of a sample of 22 spiral galaxies to study the correlation between the far infra-red (FIR) and RC emissions within the galactic disks. A combination of exponential and gaussian profiles rather than a single exponential profile is found to be a better representation of the observed intensity profiles in the two bands. The gaussian component, which we show is not due to the effects of limited beam-resolution, contains more than 60% of the total flux in majority of the galaxies. The dominance of the gaussian component suggests that the nuclear star forming regions and the bulge stars are more important contributors to the emission in the two bands, rather than the outer exponential stellar disks. The RC profile is flatter compared to the FIR profile, resulting in a decrease of their ratio,  $Q_{60}$ , away from the center. However, the  $Q_{60}$  increases in the extreme outer parts, where the dispersion in the FIR and RC correlation is also higher than in the central regions. The global  $Q_{60}$  and its dispersion match those in the inner parts of the galaxies. These results imply that the observed tight correlation in the global quantities reflects processes in the inner regions only where OB stars and the associated Type II supernovae control the FIR and RC emission. In the outer parts heating of very small dust grains by the old disk stars provides a secondary component in the FIR emission, without associated RC emission.

The edge-on galaxy NGC 3079 shows extended FIR and RC emissions along its minor axis, probably associated with the nuclear starburst activity.

*Subject headings:* star formation – far infrared emission — radio continuum emission

## 1. Introduction

In recent years considerable efforts have been put in to improving the resolution of images obtained with the Infrared Astronomical Satellite (IRAS) by using different deconvolution techniques (Aumann et al. 1990; Ghosh et al. 1993). The resultant resolutions enable the study of the physical properties within galaxies over kpc scales in nearby galaxies. Devereux and collaborators have made use of these high resolution images to establish a good spatial correspondence between the deconvolved IRAS images of the nearest galaxies and indicators of massive star formation as traced by H $\alpha$  emission line (M31: Devereux et al. 1994; M101: Devereux & Scowen 1994, M81: Devereux et al. 1995). At the presently available resolution, the distribution of various physical quantities related to the far infrared emission can be studied within galaxies at least up to the distance of the Virgo Cluster. We here undertake such a study and intend to find answers to the following questions:

1. Does the correlation seen between the global far infrared (FIR) and radio continuum (RC) emissions extend to local scales within galaxies?

2. How is the warm dust temperature distributed within galaxies? How significant are the contributions of the bulge and disk stars in heating the dust?
3. How is the dust mass distributed within galaxies? How is it related to the gas mass?

The above questions become particularly important considering the present understanding in this field based on global fluxes, which are summarized below.

1. The observed correlation between the FIR and RC fluxes can be understood in terms of phenomena associated with massive star formation, but the tightness of the correlation remains a puzzle.
2. While a majority of investigators believe the heating of dust by ultraviolet photons from young stars as a predominant source of the FIR emission (Helou et al. 1985; Sanders et al. 1986; Rengarajan & Verma 1986; Devereux et al. 1994), there have also

been discussions on the role of heating by non-ionizing photons from the bulge and disk stars (Walterbos & Schwering 1987; Smith et al. 1994; Xu & Helou 1996).

3. Global data reveal gas-to-dust mass ratios in galaxies are around 5–6 times the value in the local Galactic surroundings (Devereux & Young 1990).

We have undertaken a comprehensive study of spiral galaxies based on the available published data of the distribution of gas and RC emission in addition to IRAS data at  $\sim 1'$  resolution. The first of the questions above is addressed in the present paper, while the other two questions are addressed in a companion paper (Mayya & Rengarajan 1997; Paper II henceforth). The sample and analysis method adopted are discussed in sec. 2. In sec. 3, we present and discuss the 2-dimensional maps of the RC and  $60\mu\text{m}$  emission along with the fits to the azimuthally averaged radial intensity profiles. The variations in the  $60\mu\text{m}$  to RC flux ratio within the galaxies are also presented in this section. Issues related to the FIR-RC correlation are discussed in Sec. 4. One of the program galaxies (NGC 3079) shows a possible FIR halo, which is discussed in sec. 5. The main results of this study are summarized in sec. 6. Preliminary results based on a smaller sample have been presented by us earlier (Mayya & Rengarajan 1996).

## 2. The sample, data and analysis procedure

We aim to study the distribution of the FIR emission within disk galaxies and its relationship with the RC emission, heating sources and the distribution of gas mass. Accordingly a list of spiral galaxies is drawn for which the following data are already available in a form convenient to use.

1. 20 cm RC images from the Very Large Array (VLA) at  $1'$  resolution (D configuration).
2. Radial surface density profiles of HI and H $_2$  at a spatial resolution of  $\sim 1'$ , either in tabular form or as radial plots.
3. Optical angular diameter  $> 5'$ .

#### 4. $60\mu\text{m}$ flux density $> 5$ Jy.

The last two criteria together ensure that there are a significant number of resolution elements in each image, and that the galaxies are bright enough in the IRAS bands to get a reliable High Resolution (HiRes) image. These selection criteria resulted in a sample of 22 spiral galaxies with a mean distance of 11 Mpc. The sample is not complete, but is representative of galaxies with a mean resolution of 3 kpc. The nearest of the galaxies such as M31 and M33 offer ten times better spatial resolution but we did not consider using them in order to have a uniform spatial resolution in the sample galaxies. The basic properties of the sample galaxies are given in Table 1. The galaxy type,  $B$  band magnitude, the optical diameter at  $25 \text{ mag arcsec}^{-2}$  in arcmins, the axis ratio  $b/a$  and the position angle of the major axis have been taken from the *Third reference catalogue of bright galaxies* (de Vaucouleurs et al. 1991; RC3 henceforth). Distances are taken from the Nearby Galaxy Catalog (Tully 1988), wherein a Hubble constant of  $75 \text{ km s}^{-1} \text{ Mpc}^{-1}$  is assumed. The  $60\mu\text{m}$  beam size expressed in arcsec is the final resolution achieved after HiRes processing.  $S_{60}$  and  $Q_{60}$  denote the total  $60\mu\text{m}$  flux density and the ratio of total  $60 \mu\text{m}$  to 20 cm fluxes respectively. The table also contains FIR and RC diameters for individual galaxies, which will be discussed later.

We acquired the HiRes images (Rice 1993) of the program galaxies in four IRAS bands from the Infrared Processing and Analysis Center. HiRes uses Maximum Correlation technique (Aumann et al. 1990), which is designed to recover the spatial information contained in the overlapping detector data samples of the IRAS all-sky survey scans. The final resolution is around  $1'$  at  $60$  and  $100\mu\text{m}$  wavelengths. Resolution is better at  $12$  and  $25\mu\text{m}$  bands, but the sensitivities in these bands are too poor to trace out the outer regions in most of the galaxies in our sample

and hence these images have only limited use for our study. The HiRes processing was done using the default configuration, which results in frames of  $1^\circ \times 1^\circ$  field with  $15''$  pixels. Sub-images of  $60 \times 60$  pixels are extracted for all galaxies except the nearest galaxy in the sample, NGC 2403, for which sections of size  $100 \times 100$  pixels are extracted. In all the cases images from the 20th iteration are used. The VLA D configuration radio continuum data at 1.49 GHz (20 cm), are collected for the program galaxies from the VLA data base (see Condon 1987; Condon et al. 1990). These RC images have gaussian beams of FWHM of either  $48''$ ,  $54''$  or  $60''$  for the sample galaxies and a pixel size of  $14''$ . The fields identical to the FIR images are extracted, matching the pixel sizes to  $15''$ . The central coordinates in the extracted fields correspond to the optical centers of galaxies as given in RC3. Flux scale of RC images are converted from  $\text{Jy beam}^{-1}$  to  $10^6 \text{ Jy sr}^{-1}$  (or  $\text{MJy sr}^{-1}$ ), to match the flux units of FIR images.

Surface brightness profiles of the HiRes and RC images are obtained by azimuthally averaging over elliptical annuli of  $1'$  width. The ellipticity and position angle of the annuli are chosen based on the optical data in Table 1. Alternative analysis is also done in which every pixel of  $1'$  size, which is the typical resolution element, is treated as an independent region for computing the desired quantities. In this case, all the images are smoothed with a boxcar filter of width  $5 \times 5$  pixel. The smoothed images are rebinned into  $1'$  pixels before obtaining the ratios of the images. Ratios are neglected from further analysis, if the pixel values in any one of the bands is below 3 times the root mean squares (rms) noise in the image in order to avoid ratios involving small numbers.

The routines under Image Reduction and Analysis Facility (IRAF) and Space Telescope Science Data Analysis System (STSDAS) are used in the reduction and the analysis of the data.

### 3. Spatial distribution of FIR and RC emission

In one of the early comparisons of the FIR and the RC 2-dimensional structures in galaxies, Beck & Golla (1988) found a good correlation between the RC and FIR emission within the galaxies M 31, M 33, M 101 and IC 342. The positional correspondence between the images in the two bands was also found by Bica et al. (1989) in spiral galaxies NGC 5236 and 6946. The  $1'$  resolution of the HiRes images allows such studies to be carried out on many more spiral galaxies. Marsh & Helou (1995) extracted azimuthally averaged radial profiles of the HiRes and RC images and confirmed the larger scale lengths of RC intensity profiles found in the earlier low resolution studies (Bica & Helou 1990). They fitted the RC and FIR intensity profiles with exponential functions, invoking a central unresolved source in some cases. In this section, we compare the structural correspondences between the FIR and RC images, in addition to analysing the radial intensity profiles.

#### 3.1. Two-dimensional structures

The  $60\mu\text{m}$  and 20 cm surface brightness contour maps of the program galaxies are reproduced in Fig. 1. The images are aligned with north at the top and east on the left. The tick marks on the plot boundary are in pixel units ( $15''$ ). The horizontal bar at the bottom-left corner corresponds to a spatial scale of 5 kpc at the assumed distances to the galaxies. The highest and lowest contour values (in  $\text{MJy sr}^{-1}$ ) are marked on the bar chart on the right hand side of each panel. Starting with the peak value as maximum, consecutive contours are scaled down by factors of two until reaching a value which is around one sigma above the background. This resulted in 7–10 contour levels in each plot. The optical major and minor axes are superimposed on the contour maps. The HiRes and RC beams at  $\frac{1}{2}$  and  $\frac{1}{8}$  of the peak value are shown as two concentric ellipses inside a square box on the

top-left corner of each panel. Note that the beam contours are denoted by thick lines, so as to distinguish them from the image contours when there is overlap. The beam ellipses are smaller than the corresponding image ellipses implying that the FIR and RC emitting sources are resolved. The effect of resolution on the extracted profiles is discussed in detail later in this section. Compact background sources when present are easily distinguishable on RC images, and hence no attempt is made in removing these sources from the images.

The striking resemblance between the  $60\mu\text{m}$  and 20 cm maps is easily noticeable in these maps. The major axis of the distribution in these two bands is well aligned with the optical major axis, in general. The FIR and RC derived axis ratios generally agree with the optical measurements, with one notable exception — NGC 3079 has a larger extension along the minor axis in both the FIR and RC compared to its optical value. The fact that the HiRes beam for this galaxy was among the best adds significance to the above result. This is a nearly edge-on galaxy and is known to show a variety of off-planar structures and hence a more detailed investigation of the observed FIR extension is done separately in Sec. 5. The FIR and RC sizes of the galaxies are measured at the  $0.60 \text{ MJy sr}^{-1}$  and  $0.01 \text{ MJy sr}^{-1}$  ( $\sim 1 \text{ mJy arcmin}^{-2}$ ) levels on the  $60\mu\text{m}$  and 20 cm surface brightness profiles respectively. These levels correspond to 3–6 and 2–5 times the rms noise above the local background on the FIR and RC images respectively. The resulting diameters are given in Table 1 as  $D_{\text{fir}}$  and  $D_{\text{rad}}$ . The sizes at these levels generally match the optical sizes at  $25 \text{ B mag arcsec}^{-2}$  ( $D_{\text{opt}}$ ). However it should be remembered that the measured sizes are overestimates due to the smearing introduced by the  $1'$  beam.

### 3.2. Decomposition of the radial intensity profiles

The azimuthally averaged radial intensity profiles at  $60\mu\text{m}$  and 20 cm are fitted with a function of the form,

$$I(r) = I_{\text{gau}} \exp(-(r/\sigma_{\text{g}})^2) + I_{\text{exp}} \exp(-r/\sigma_{\text{e}}), \quad (1)$$

where the two terms represent gaussian and exponential components respectively. The values of the four coefficients in the above equation are evaluated independently for the  $60\mu\text{m}$  and 20 cm profiles by using a least squares fitting method. The STSDAS task *nfit1d* is used for the fitting purposes. Total flux contained in each component is evaluated for the best fit parameters. We denote the flux fraction in the gaussian and exponential components by the symbols  $f_{\text{gau}}$  and  $f_{\text{exp}}$  respectively.

The results of the fit for all the galaxies are shown adjacent to the contour maps in Fig. 1. The open circles at every  $1'$  interval denote the observed profile. Gaussian and exponential components and their sum are shown by the dashed, dotted and solid lines respectively. The downward pointing arrows on the x-axis of the  $60\mu\text{m}$  plots denote the optical isophote radii of the galaxies. It can be seen that a good fit was possible throughout the optical extent of the galaxies in most cases. Each plot contains the fitted values of  $\sigma_{\text{g}}$  and  $\sigma_{\text{e}}$  in addition to  $f_{\text{gau}}$ . A missing  $\sigma$  on the plot indicates that the flux fraction in the corresponding component is less than 20%. However, we point out that there are cases where the fitted outer exponential component is reliable even when it contains less than 5% of total flux (e.g. NGC 4736). In Table 2, we give the values of  $\sigma_{\text{g}}$ ,  $\sigma_{\text{e}}$ , and  $f_{\text{gau}}$  for both the FIR and RC profiles, whenever the component seems to be distinct, irrespective of the flux fraction contained in that component. An observational scale length  $\sigma_{\text{obs}}$  is obtained by measuring the width of the observed profile at  $1/e$  of the peak intensity.  $\sigma_{\text{obs}}$  is independent

of the profile fitting and is expected to match the  $\sigma_{\text{e}}$  for a purely exponential profile. Values of  $\sigma_{\text{obs}}$  for the RC profile and its ratio with the FIR scale length are given in the last two columns. Before we discuss the significance of the two components we compare fits with two components with that obtained using only an exponential function.

#### 3.2.1. Fits with exponential component alone

Bicay & Helou (1990) and more recently Marsh & Helou (1995) assumed the intensity profiles at the FIR and RC bands to be exponential in form and obtained the scale lengths by fitting the exponential function to the observed data. They added an unresolved central source in a few cases where the galaxy is known to harbor a starburst or an active galactic nucleus. Only two of the program galaxies (NGC 3079 and 3628) in our sample are known to contain central compact sources. We fitted a single exponential function to the intensity profiles. The resultant  $60\mu\text{m}$  scale lengths are compared with that tabulated by Marsh & Helou (1995) for the eight galaxies in common, in Fig. 2. The agreement between the scale lengths is satisfactory.

However fitting only an exponential component results in higher residuals. In other words the rms departures from the fit obtained by using only an exponential function for fitting are systematically higher as compared with the 2-component fitting described above. This is illustrated in Fig. 3 where the histogram of the ratio of the residuals of exponential fits to the 2-component fits is plotted. The ratio is greater than unity in all the galaxies, except in NGC 2403, 7331 (FIR fits) and 4321 (RC fit). Thus, the addition of a gaussian component results in a better fit, as compared to pure exponential fits in majority of the program galaxies.

### 3.2.2. Beam effects on the profile decomposition

In the previous subsections, we demonstrated that the addition of a gaussian component to an exponential component results in a better fit to the observations, and that the gaussian is often the dominant component. Exponentially decreasing intensity profiles are more common in galactic disks. Hence we check whether the observed gaussian shaped profiles can be produced by the beam effects on an intrinsically exponential profile. We choose the best-fit single component exponential profile and convolve it with the beam profile of the galaxy. For the sake of simplicity, convolutions are performed on 1-dimensional profiles along the major axis of the galaxies. Four galaxies with different degrees of gaussian domination are selected for representation in Fig. 4. NGC 2903 and 5055 represent well-resolved galaxies in the sample, where as NGC 4254 and 4303 are among the galaxies with the minimum number of resolution elements. Beam-convolved exponential profiles are shown by the dotted lines; circles represent the observed profile, and the beam is shown by a dot-dashed line. For comparison, the best-fit 2-component profile is plotted as a solid line. The percentage of the total flux in the gaussian component and the ratio of the rms errors of the single-exponential to the 2-component fit are noted in each panel. It can be inferred from the plots that the beam-convolved exponential profile is only marginally different from the exponential profile, which will appear as a straight line on the plot. In galaxies with a dominant gaussian component, the observed profiles are closer to the gaussian rather than the convolved exponential, independent of the resolution. In galaxies with  $f_{\text{gau}} < 0.5$ , the gaussian component can be an artifact of poorer resolution, but in those galaxies with larger  $f_{\text{gau}}$ , the gaussian component must be due to an intrinsically gaussian disk.

It is further noted that there are purely exponential-shaped profiles among the poorly-resolved galaxies, and gaussian-dominant profiles among the well-resolved

galaxies. This indicates that the profile shapes are independent of resolution. From all these discussions we conclude that the gaussian component is definitely not due to an artifact of poorer spatial resolution, whenever the component contains more than  $\sim 60\%$  of the total flux.

### 3.3. Implications of the two components

It can be seen in Table 2 that the gaussian component is significant (i.e.  $f_{\text{gau}} > 0.6$  in either FIR or RC) in 17 of the 22 galaxies. The five galaxies in which the component is insignificant are, NGC 3079, 3198, 4321, 4656 and 6946. The gaussian component stands out distinctly more often in the RC than in the FIR. There are 13 galaxies with more than 80% of the flux in the gaussian component in the RC compared to 5 in the FIR. The mean flux fraction in the gaussian component is  $0.62 \pm 0.25$  in the FIR, where as it is  $0.70 \pm 0.33$  in the RC. The mean of the difference  $f_{\text{gau}}(\text{RC}) - f_{\text{gau}}(\text{FIR}) = 0.08 \pm 0.30$ . The reason for  $f_{\text{gau}}$  being greater than  $f_{\text{exp}}$  on an average may be that it is fitted as a central component in a profile which increases steeply towards the center.

We now investigate the physical origin of the gaussian component. Firstly, we examine whether this component is due to an unresolved central source. The ratio of full width at half maximum (FWHM) of the gaussian component to the point source FWHM is plotted in Fig. 5. The gaussian component is clearly resolved both in the FIR and RC; thus a central point source cannot be responsible for the gaussian component. Hence we examine a possible relationship between the basic galaxy parameters and the strength of the gaussian component. The flux fraction in the gaussian component is plotted as a function of Hubble type and inclination in Fig. 6 for the RC and FIR separately. Barred, unbarred and intermediate galaxy types are distinguished by using different symbols. To within errors we see no effect of the bar or inclination. As a function of Hubble type also, there is no clear de-

pendence. However, the lower envelope of the spread seems to decrease with increasing Hubble type. The latest type spiral in our sample is NGC 4656 (T=9) and the gaussian fraction for this is  $< 0.1$  in both the bands. Hence the bulge, which is absent in late type galaxies, may have a role to play in creating a gaussian component.

Smith et al. (1994) have established that the observed dust temperatures in the central regions of NGC 4736 and 3627 cannot be reproduced by the inferred massive stars there or by the nuclear activity, where as bulge stars can easily do the heating because of their large number. Our sample includes both of these galaxies and both show strong gaussian components in both the FIR and RC emission. Thus it is likely that the bulge stars are primarily responsible for producing non-negligible FIR luminosity in the gaussian component. This implies that the gaussian strength should decrease with Hubble type, in agreement with the trend seen in Fig. 6. There may be additional sources present in some galaxies, leading to the scatter in the correlation between the gaussian strength and the bulge strength. The most likely candidates for these additional sources are the circumnuclear star forming regions, which have typical sizes of 1–2 kpc. The gaussian component may also be accentuated by the steep gradient of gas (and hence dust) towards the center in the FIR as observed for several galaxies (Young & Scoville 1991). In the radio continuum the increased magnetic field in the central region may contribute to the dominance of the gaussian component.

The ratio of the observed scale lengths of the RC and FIR intensity profiles (last column in Table 2) is plotted against the fractional flux contained in the gaussian component in Fig. 7. The RC profiles are found to be broader than the FIR profiles in all but four galaxies (NGC 3628, 4192, 4321, 4569). The mean value of the ratio  $\sigma_{\text{obs}}(\text{RC})/\sigma_{\text{obs}}(\text{FIR}) = 1.22 \pm 0.22$ . The FIR and RC profiles have mean scale

lengths of 5.0 kpc and 5.9 kpc respectively. The four galaxies with lower RC scale length, as compared to that of FIR, behave differently from the rest in the radial distribution of  $Q_{60}$ . This will be discussed in the next sub-section.

The higher scale length for the RC as compared to that for the FIR is consistent with the findings of Bica & Helou (1990) and Marsh & Helou (1995). The larger scale length of the RC is believed to be a consequence of the diffusion of radio emitting electrons away from the place of origin, viz. supernova remnants around the Type II supernovae from OB stars in the disc. In 6 galaxies viz. NGC 2903, 3198, 3628, 4736, 5033 and 7331, we find that besides the central gaussian component, an exponential component is also present at radii greater than  $\sim 5$  kpc in both the FIR and RC profiles. It is mostly a minor component in terms of the contribution to the total flux, but has higher flux than the gaussian component at radii exceeding 5 kpc. In four of these six galaxies the exponential scale length for FIR exceeds the RC scale length. This implies that the FIR emission drops more slowly than the RC emission in the outer regions of the galaxies. This is also confirmed by the fact that in our sample of 22 galaxies, 20 have a FIR exponential component in addition to a central gaussian component whereas only 10 have this additional component in RC. This effect is also seen in the radial profile of  $Q_{60}$ , the ratio of emission at  $60\mu\text{m}$  to that in the RC, as discussed below.

### 3.4. Variation of $Q_{60}$ within galaxies

A ratio involving the fluxes in the FIR and the RC wavelengths is useful in assessing the tightness of the correlation between the two quantities within a given galaxy. Accordingly we define  $Q_{60}$  as the ratio of emission at  $60\mu\text{m}$  to that at 20 cm. We construct the 1-dimensional profile as well as the pixel map of  $Q_{60}$ .

Azimuthally averaged radial profiles in  $60\mu\text{m}$  and

20 cm surface brightness are used to obtain the radial profiles of  $Q_{60}$ .  $Q_{60}$  is found to decrease by only a factor of around 3 in a given galaxy, in spite of FIR and RC intensities falling by several orders of magnitude. This result is consistent with the findings of Bica & Helou (1990). The variation of  $Q_{60}$  is understood in terms of the larger RC scale length, compared to the FIR scale length.  $Q_{60}$  values in individual galaxies are plotted in Fig. 8, both as a function of  $60\mu\text{m}$  surface brightness ( $I_{60}$ ) and the radial distance from the center. Note that  $I_{60}$  increases towards the left, so that the  $Q_{60}$  vs  $I_{60}$  plot can be directly compared with the radial gradients in  $Q_{60}$  shown on the adjacent plots. The open circles represent values over  $1'$  pixels, whereas the thin solid line ( $Q_{60}$  vs  $I_{60}$ ) and thick solid line connecting filled circles ( $Q_{60}$  vs  $R/R_{25}$ ) show the azimuthally averaged profiles. The  $Q_{60}$  values obtained from the global data are indicated by the dotted horizontal line.  $Q_{60}$  shows a tendency to decrease away from the center in all galaxies except in NGC 4192, 4321 and 4569. In NGC 3628, the  $Q_{60}$  peak is shifted by  $1'$  away from the nucleus. Note that these are the four galaxies in which the FIR scale length is larger than the RC scale length.  $Q_{60}$  obtained from the global data, in general, correspond to the values in the central regions of galaxies. This is an indication to the fact that the global quantities are flux weighted and hence represent the properties of high intensity central regions. It is interesting to note that the galaxies NGC 628 and 2403 do not have a well defined central peak in the distribution of FIR and RC intensity, and their global  $Q_{60}$  values match the mid-disk values rather than the central values.

In 13 galaxies,  $Q_{60}$  reaches a minimum around  $R/R_{25} \sim 0.5$  and then either increase or remain flat. It is significant to note that this behavior is shown by all galaxies which have an outer exponential FIR component without a corresponding RC counterpart. In 6 galaxies, viz. NGC 4192, 4321, 4569, 4736, 5033 and 7331, the outermost  $Q_{60}$  value is larger than the

central value. Results presented in the companion paper (Paper II) help us to understand the detailed behavior of the  $Q_{60}$  profiles, which is the topic of the next section.

#### 4. Discussion on the FIR-RC correlation

The tightness of the correlation between the RC and FIR intensities depends on the sources responsible for their emissions and the life times of these sources determine the time scales for contribution to the emission. The closer the two time scales, the tighter is the correlation (Rengarajan & Iyengar 1990). The FIR emission originates from dust grains which are heated by the ultraviolet photons from young OB stars and long-lived intermediate mass stars (Walterbos & Greenawalt 1996). It is known that the various features in the interstellar extinction curve can be explained only by a mixture of classical big grains (BGs), very small grains (VSGs) and long molecular chains such as polycyclic aromatic hydrocarbons (PAHs) (see Désert et al. 1990). VSGs absorb photons and get heated temporarily to about 100 K, independent of photon energy and flux. Hence the FIR emission is proportional to the recent star formation rate only if the emission from BGs dominates the total FIR emission. Applying the model of Désert et al. (1990), we find that the contribution of the BGs to the total  $60\mu\text{m}$  emission systematically decreases away from the center; the contribution is less than 50% at radii larger than half the disk radius (Paper II). Thus the FIR emission is more closely tied to recent star formation rate (SFR) in the inner regions compared to the outer regions.

What about the RC emission? Assuming that the sources of radio continuum emitting cosmic ray electrons are supernovae (SN), the progenitor stars of SN determine the time scale of contribution. Type II SN originate from massive OB stars while Type I SN result from less massive and long-lived stars (Trimble 1985). Rengarajan & Iyengar (1990) have argued that



the tight correlation between the global FIR and RC emissions implies that the Type II SN contribution dominates. This is consistent with the observation of van den Bergh et al. (1987) that the frequency of Type I SN in spiral galaxies is only one fourth the frequency of Type II SN. Thus the RC emission is directly related to the massive SFR.

Both the FIR and RC emissions are controlled by the recent star formation only in the inner parts of the galaxies. In the outer parts, transiently heated VSGs provide a source of FIR emission independent of the local SFR. This explains the lower gradient of the FIR profile and the increase of  $Q_{60}$  in the outer regions of galaxies. Dispersion on the correlation is also expected to be higher in the outer parts. We demonstrate in Fig. 9 that this is indeed the case for our sample of galaxies. Local  $Q_{60}$  values at 25, 50, 75 and 100% of the disk radius are plotted in the top panel. Individual galaxies are denoted by open circles at each of the four radial positions, with their mean values joined by solid lines. The rms values (in log units) over these mean values are noted on the plots. Values 1-rms above and below the mean are denoted by the dotted lines. Galaxies with the largest deviations from the mean  $Q_{60}$  are identified by their NGC numbers. The dispersion is found to remain constant at 0.20 dex inside half the disk radius; the dispersion increases to 0.49 dex at the outer edges of the optical disk.

Is the global correlation affected by the higher dispersion in the outer parts of galaxies? In order to answer this question we computed the  $Q_{60}$  values by dividing the FIR and RC fluxes over progressively increasing radial zones. The results are plotted in the lower panel of Fig. 9. The dispersion of 0.20 dex in the global value corresponds to the dispersions in the inner half of the disk. We have noted earlier that the global  $Q_{60}$  values represent the values in the inner parts of the galaxies. Thus the tightness in the global correlation only requires the correlation to be tight in

individual bright regions.

## 5. FIR halo in NGC 3079?

The FIR and RC emissions along the minor axis of NGC 3079 extend beyond the optical disk. The stellar disk of this galaxy is oriented nearly edge-on and hence the larger minor axis extension implies a larger scale height (or a halo) of the FIR emitting dust, and radio emitting electrons. RC halos have been noticed in several edge-on galaxies (Hummel et al. 1991), but we have seen no reports of FIR halos. There has been indirect evidence for the presence of dust in the halos of galaxies based on the line of sight optical depth towards distant quasars (Zaritsky 1994). Since dust grains are formed in the disks of galaxies, one needs a physical mechanism for their transport to the halo. Before we discuss the possible ways by which dust can be carried and maintained in the halos of galaxies, we shall look into the dust temperature distribution along the major and minor axes of this galaxy. The galaxy is a bright FIR source, and hence the  $25\mu\text{m}$  image is also used in the analysis. We compare the minor axis flux profiles in 25, 60 and  $100\mu\text{m}$  bands with their beam profiles along the same direction in the top three panels of Fig. 10. These plots indicate that the observed minor axis structures are resolved. The FIR flux ratios  $f_{25}/f_{60}$  and  $f_{60}/f_{100}$ , which are indicators of dust temperatures, are plotted along the two axes of the galaxy in the bottom-most panel of Fig. 10. The observed points, which are averages over  $1'$  regions, are joined by lines to illustrate the difference in the gradients along the two axes. The FIR flux ratios, especially the one involving  $25\mu\text{m}$  (the hotter dust), falls off faster along the minor axis. This is consistent with the picture that the heating sources are in the disk and hence the halo dust must be cooler than that in the disk.

Non-thermal RC halos have been interpreted in terms of the escape of cosmic ray electrons away from the disk of galaxies along the open magnetic field lines

or inflated flux tubes (see Parker 1992). In recent years, vertical dust structures extending up to several kpc, thought to be tracing the magnetic field lines, have been noticed in several galaxies (Sofue 1987). Using the computations of Franco et al. (1991), Sofue et al. (1994) have shown that the radiation pressure due to star light from the disk and bulge, particularly from starburst regions, would drive the dust grains (associated with partially ionized gas) along vertical magnetic tubes producing vertical dust structures for magnetic fields stronger than a few  $\mu\text{G}$ . Central regions of starburst galaxies are preferred regions for the formation of vertical structures, due to their strong radiation pressure as well as the magnetic field strength. The ejected gas and dust fall back into the disk at various radial zones, thus enriching the halo with dust and gas on a global scale.

NGC 3079 has been the target for the detection of extra-planar structures in different bands. de Bruyn (1977) and Hummel et al. (1983) detected radio continuum features normal to the plane of the galaxy. Irwin et al. (1987) and Duric & Seaquist (1988) detected a wind associated with strong magnetic fields. The galaxy is among a few objects which show biconic ionized filaments centered around the nucleus — a manifestation of violent starburst activity in the galactic nucleus (Heckman et al. 1990). NGC 3079 is known to contain diffuse ionized gas (DIG) extending to several kpc in the halo (Veilleux et al. 1995). Thus, NGC 3079 satisfies all the conditions for the presence of warm dust in its halo. However, it is interesting to note that, NGC 3628, another edge-on galaxy in the sample also shows evidence for the presence of nuclear superwinds (Fabbiano et al. 1990), but does not show any trace of FIR halo.

## 6. Conclusions

Azimuthally averaged radial intensity profiles in  $60\mu\text{m}$  and 20 cm continua bands are analyzed in a sample of 22 spiral galaxies. A combination of gaussian

and exponential components is found to fit the observed radial intensity profiles in the two bands better than the conventional exponential component alone. The majority of the galaxies contain more than 60% of the flux in the central gaussian component in both the bands. The sample galaxies show a predominantly gaussian component more often in the RC than in the FIR. The RC scale lengths are larger than the FIR scale lengths, which results in a radial decrease of  $Q_{60}$ , the flux ratio in the two bands. In a significant number of the galaxies,  $Q_{60}$  remains flat or increases beyond half the disk radius, which is caused by the outer exponential component in the FIR without a RC counterpart. The tightness of the global FIR-RC correlation is determined by the processes in the inner regions only. All the observed properties can be understood by a model in which the kpc-scale nuclear star forming regions and the bulge stars are responsible for the FIR and RC emission in the central parts. The very small grains heated by the old disk stars dominate the FIR emission, without contributing to RC emission due to the lack of Type II supernovae, in the outer galaxies.

The edge-on galaxy NGC 3079 shows FIR and RC halos, possibly associated with the nuclear starburst activity.

It is a pleasure to thank Dr. Walter Rice, the referee, for his comments and suggestions towards improvement of the manuscript. We thank Dr. J.J. Condon for supplying the CDROM containing RC data of galaxies, which formed the basis of this work. I (ydm) thank Dr. S.K. Ghosh for introducing me to the IRAS data-base and also to the various pipelines run by IPAC. TNR thanks Dr. G.G.Fazio and the hospitality of Smithsonian Astrophysical Observatory, Cambridge, USA where part of this work was done as a Short Term Visitor. This research has made use of the NASA/IPAC Extragalactic Database (NED) which is operated by the Jet Propulsion Laboratory, Califor-

nia Institute of Technology, under contract with the  
National Aeronautics and Space Administration.

## REFERENCES

- Aumann, H.H., Fowler, J.W., & Melnyk, M., 1990, AJ 99, 1674
- Beck, R., & Golla, G., 1988, A&A 191, L9
- Bicay, M.D., & Helou, G., 1990, ApJ 362, 59
- Bicay, M.D., Helou, G., & Condon, J.J., 1989, ApJ 338, L53
- Condon, J.J., 1987, ApJS 65, 485
- Condon, J.J., Helou, G., Sanders, D.B., & Soifer, B.T., 1990, ApJS 73, 359
- de Bruyn, A.G., 1977, A&A 58, 221
- Désert, F.-X., Boulanger, F., & Pugget, J.L., 1990, A&A 237, 215
- de Vaucouleurs, G., de Vaucouleurs, A., Corwin, H.G., et al. 1991, Third Reference Catalogue of Bright Galaxies (New York: Springer-Verlag)(RC3)
- Devereux, N.A., Scowen, P.A., 1994, AJ 108, 1244
- Devereux, N.A., Young, J.S., 1990, ApJ 359, 42
- Devereux, N.A., Jocoby, G., & Ciardullo, R., 1995, AJ 110, 1115
- Devereux, N.A., Price, R., Wells, L.A., & Duric, N., 1994, AJ 108, 1667
- Duric, N., & Seaquist, E.R., 1988, ApJ 326, 574
- Fabbiano, G., Heckman, T.M., & Keel, W.C., 1990, ApJ 355, 442
- Franco, J., Ferrini, F., Ferrara, A. & Barsella, B., 1991, ApJ 366, 443
- Ghosh, S.K., Verma, R.P., Rengarajan, T.N., Das, B. & Saraiya, H.T., 1993, ApJS 86, 401
- Heckman, T.M., Armus, L., & Miley, G.K., 1990, ApJS 74, 833
- Helou, G., Soifer, B.T., & Rowan-Robinson, M., 1985, ApJ 298, L7
- Hummel, E., Beck, R., & Dettmar, R.-J., 1991, A&AS 87, 309
- Hummel, E., van Gorkom, J.H., & Kotanyi, C.G., 1983, ApJ 267, L5
- Irwin, J.A., Seaquist, E.R., & Duric, N., 1987, ApJ 313, L91
- Marsh, K.A. & Helou, G., 1995, ApJ 445, 599
- Mayya, Y.D. & Rengarajan, T.N., 1996, in IAU Symposium 171, New Light on Galaxy Evolution, ed. R. Bender & R.L. Davies (Kluwer), 415.
- Mayya, Y.D., & Rengarajan, T.N., 1997, (Paper II)
- Parker, E.N., 1992, ApJ 401, 137
- Rengarajan, T.N., & Iyengar, K.V.K., 1990, MNRAS 242, 74
- Rengarajan, T.N., & Verma, R.P., 1986, A&A 165, 300
- Rice, W., 1993, AJ 105, 67
- Sanders, D.B., Scoville, N.Z., Young, J.S., et al. 1986, ApJ 305, L45
- Smith, B.J., Harvey, P.M., Colome, C., Zhang, C.Y., & Difrancesco, J., 1994, ApJ 425, 91
- Sofue, Y., 1987, PASJ 39, 547
- Sofue, Y., Wakamatsu, K., & Malin, D.F., 1994, AJ 108, 2102
- Trimble, V., 1985 in Supernovae, their Surroundings and Remnants, ed. Srinivasan, G., & Radhakrishnan, V., J.Astroph. Astr. Suppl. (Bangalore: Ind. Acad. Sci.), 9
- Tully, B.R., 1988, Nearby Galaxies Catalog, Cambridge Univ. Press

van den Bergh, S., McClure, D.R., & Evans, R., 1987,  
ApJ 323, 44

Veilleux, S., Cecil, G., & Bland-Hawthorn, J., 1995,  
ApJ 445, 152

Walterbos, R.A.M., & Schwing, P.B.W., 1987, A&A  
180, 27

Walterbos, R.A.M., & Greenawalt, B., 1996, ApJ 460,  
696

Xu, C., & Helou, G., 1996, ApJ 456, 152

Young, J.S., & Scoville, N.Z., 1991, ARA&A 29, 581

Zaritsky, D., 1994, AJ 108, 1619

TABLE 1  
BASIC DATA ON SAMPLE GALAXIES

NGC	Type	$B_T^0$	dist Mpc	$S_{60}$ Jy	$Q_{60}$	60 $\mu$ m beam " x "	Diameter (')			b/a opt	PA ( $^\circ$ ) opt
							opt	fir	rad		
628	SA(s)c	9.76	9.7	25.5	142	77 x 42	10.47	9.0	10.0	0.91	25
2403	SAB(s)d	8.43	4.2	62.6	190	60 x 42	21.88	15.5	12.5	0.56	127
2841	SA(r)b	9.58	12.0	6.3	75	79 x 45	8.13	7.3	8.5	0.44	147
2903	SAB(rs)bc	9.11	6.3	67.6	166	68 x 45	12.59	13.3	10.0	0.48	17
3079	SB(s)c	10.41	20.4	52.8	62	40 x 35	7.94	6.0	6.5	0.18	165
3198	SB(rs)c	10.21	10.8	6.9	250	67 x 32	8.51	8.0	7.0	0.39	35
3627	SAB(s)b	9.13	6.6	66.5	145	72 x 42	9.12	12.0	9.5	0.46	173
3628	ScP	9.31	7.7	56.9	108	86 x 35	14.79	12.5	14.0	0.20	104
4192	SAB(s)ab	10.02	16.8	8.4	114	92 x 45	9.77	11.5	10.0	0.28	155
4254	SA(s)c	10.10	16.8	40.7	96	64 x 43	5.37	6.8	7.0	0.87	0
4303	SAB(rs)bc	10.12	15.2	40.2	97	83 x 45	6.46	6.3	7.5	0.89	0
4321	SAB(s)bc	9.98	16.8	26.9	79	55 x 35	7.41	7.0	6.5	0.85	30
4501	SA(rs)b	9.86	16.8	20.7	75	61 x 44	6.92	6.5	7.0	0.54	140
4535	SAB(s)c	10.32	16.8	12.6	195	62 x 44	7.08	7.8	7.5	0.71	0
4569	SAB(rs)ab	9.79	16.8	11.0	132	84 x 44	9.55	8.0	5.0	0.46	23
4656	SB(s)mP	10.10	7.2	7.0	112	76 x 44	15.14	14.0	14.0	0.20	33
4736	RSA(r)ab	8.75	4.3	75.2	296	63 x 42	11.22	5.8	5.5	0.81	105
5033	SA(s)c	10.21	18.7	21.6	121	65 x 43	10.72	8.5	7.5	0.47	170
5055	SA(rs)bc	9.03	7.2	50.9	131	61 x 42	12.59	10.0	9.5	0.58	105
6503	SA(s)cd	10.11	6.1	11.1	304	67 x 44	7.08	8.3	7.5	0.34	123
6946	SAB(rs)cd	7.78	5.5	165.2	118	39 x 35	11.48	11.8	14.0	0.85	32
7331	SA(s)b	9.38	14.3	41.9	112	75 x 43	10.47	14.0	11.0	0.36	171

TABLE 2  
RESULTS OF FITS TO THE RADIAL PROFILES OF GALAXIES<sup>1</sup>

NGC	FIR			RC			$\sigma_{\text{obs}}(\text{RC})$	$\frac{\sigma_{\text{obs}}(\text{RC})}{\sigma_{\text{obs}}(\text{FIR})}$
	$\sigma_{\text{g}}$	$\sigma_{\text{e}}$	$f_{\text{gau}}$	$\sigma_{\text{g}}$	$\sigma_{\text{e}}$	$f_{\text{gau}}$		
628	6.5	...	0.90	8.2	...	1.00	9.49	1.42
2403	3.6	2.7	0.64	4.4	...	0.88	4.39	1.29
2841	7.6	...	1.00	8.9	...	1.00	8.76	1.10
2903	2.5	4.2	0.93	3.3	1.8	0.52	2.78	1.20
3079	12.9	6.9	0.18	16.1	9.1	0.45	12.41	1.41
3198	4.9	4.6	0.60	6.2	4.4	0.28	5.56	1.17
3627	3.1	2.5	0.76	3.9	...	1.00	4.00	1.34
3628	4.6	2.6	0.74	5.2	3.0	0.24	3.72	0.91
4192	13.9	4.8	0.63	12.0	7.4	0.74	11.41	0.98
4254	5.2	3.3	0.59	7.9	...	0.88	6.87	1.48
4303	5.1	6.2	0.94	6.4	...	1.00	6.30	1.23
4321	5.9	3.7	0.35	...	3.1	0.00	4.33	0.85
4501	6.2	3.5	0.69	7.4	...	0.98	7.47	1.31
4535	6.1	3.8	0.31	9.2	...	0.84	6.14	1.20
4569	6.2	5.4	0.56	5.8	...	0.99	5.75	0.90
4656	...	5.4	0.05	...	6.6	0.08	5.95	1.17
4736	1.0	3.4	0.98	1.5	1.4	0.95	1.57	1.88
5033	5.3	5.8	0.65	6.6	4.5	0.58	6.11	1.16
5055	3.1	2.1	0.44	4.9	...	0.82	3.69	1.33
6503	3.2	1.6	0.66	3.6	...	0.91	3.56	1.28
6946	1.1	1.7	0.39	0.9	2.3	0.20	1.50	1.14
7331	7.7	6.3	0.47	9.1	8.1	0.89	8.83	1.19

<sup>1</sup> $\sigma_{\text{g}}$  and  $\sigma_{\text{e}}$  are in kpc.  $\sigma_{\text{obs}}(\text{RC})$  and  $\sigma_{\text{obs}}(\text{FIR})$  are the widths of the observed profiles measured at 1/e of the peak intensity.

Fig. 1.—  $60\mu\text{m}$  and 20 cm emission contours and azimuthally averaged intensity profiles of 22 galaxies are shown. The maximum and minimum contour levels in units of  $\text{MJy s}^{-1}$  are indicated on the bar chart at the right hand side of each contour plot. Starting with the peak intensity, successive contours differ by a factor of two. The HiRes and RC beams at  $\frac{1}{2}$  and  $\frac{1}{8}$  of the peak level are shown as two concentric ellipses at the top-left corner of each panel. The horizontal bar at the bottom-left corner corresponds to a linear scale of 5 kpc within the galaxies at the assumed distances. The optical major and minor axes are shown by a cross centered on the galaxy image. The coordinate system of the contour plots is in pixel units ( $15''$ ). The two panels on the right hand side depict the observed intensity profiles at  $60\mu\text{m}$  and 20 cm, along with the two-component fits described in the text. Circles represent the observed values sampled at every  $1'$ , where as the dashed and dotted lines represent gaussian and exponential component of the fit respectively. The solid lines represent the sum of the two components. The most important parameters obtained from the fit are indicated. The downward pointing arrow on the radius axis of  $60\mu\text{m}$  radial profile denotes the optical radius for each galaxy.



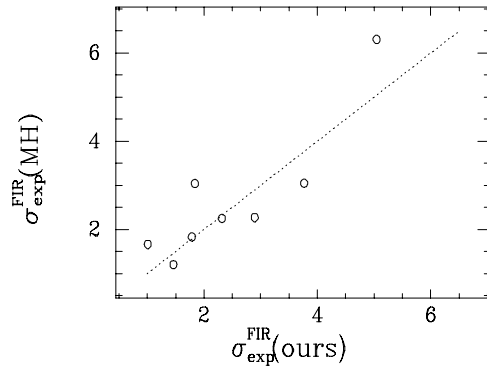


Fig. 2.— The exponential scale length (in kpc) for the FIR emission as tabulated by Marsh & Helou (1995) is plotted against the value obtained by us for the single exponential component for the 8 galaxies in common. The dotted line corresponds to a unity-slope line passing through the origin.

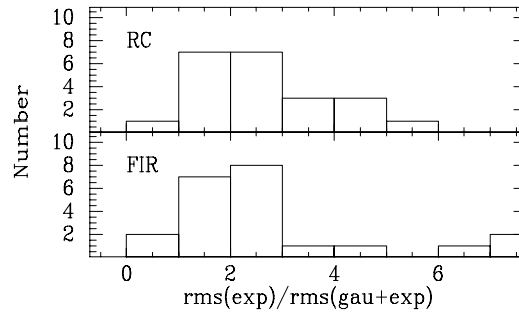


Fig. 3.— The root mean squares (rms) residuals from the 2-component fits, shown in Fig. 1, are compared with the rms residuals obtained by one-component (exponential) fits. Except for two galaxies in FIR (NGC 2403, 7331) and one in RC (NGC 4321), the ratio is greater than unity, implying the necessity of a gaussian component in addition to the exponential component to represent the emission profiles in the FIR and RC bands.

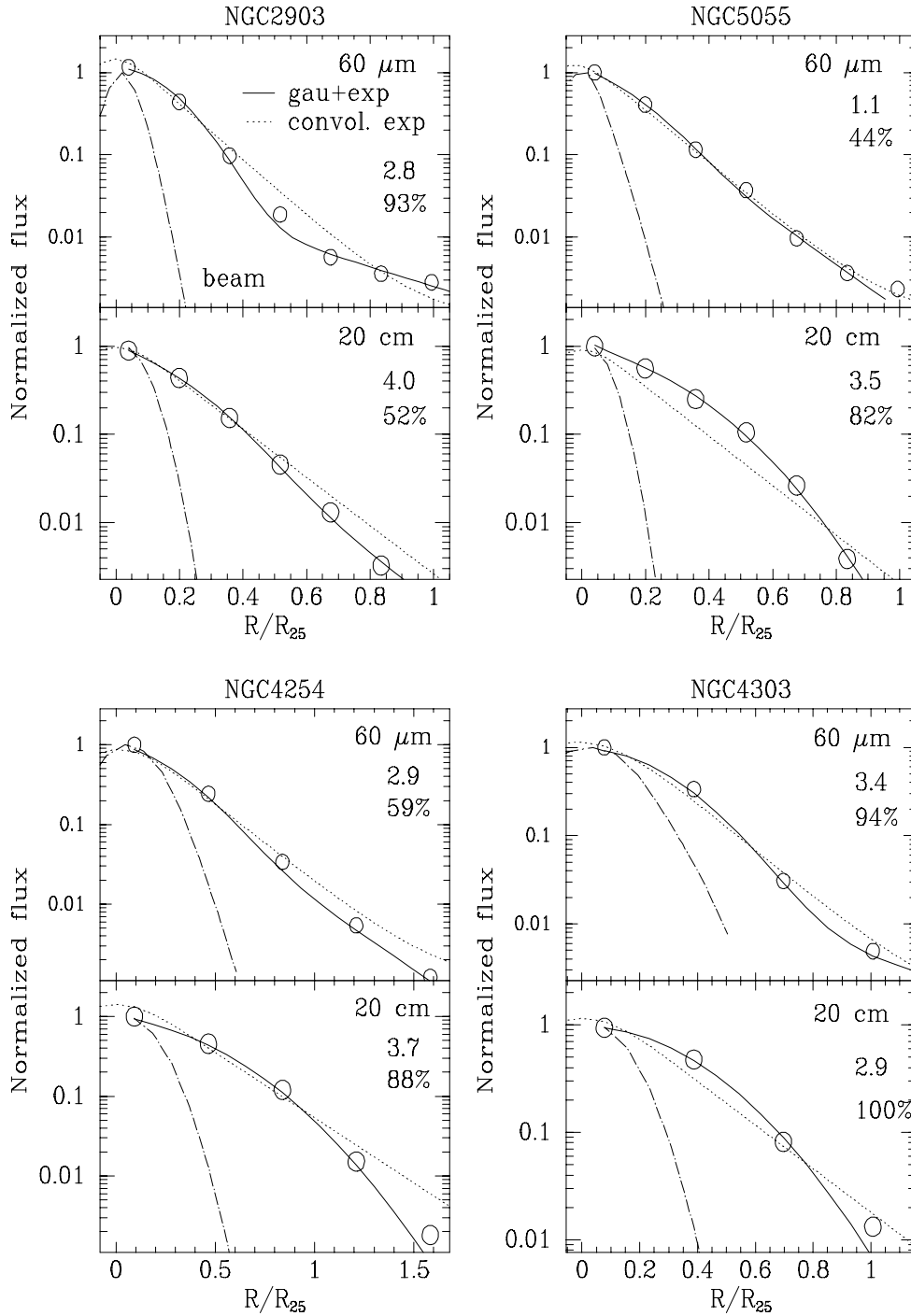


Fig. 4.— The beam-convolved exponential profile (dotted line) is compared with the best-fit 2-component profile (solid line) and observations (circles). The beams used for convolution are shown by dot-dashed lines. The ratio of the rms errors of the single exponential component to that of the 2-component and the percentage flux in the gaussian component are indicated on the plot. NGC 2903 and 5055 represent well-resolved galaxies, where as NGC 4254 and 4303 represent marginally resolved galaxies. See text for details.

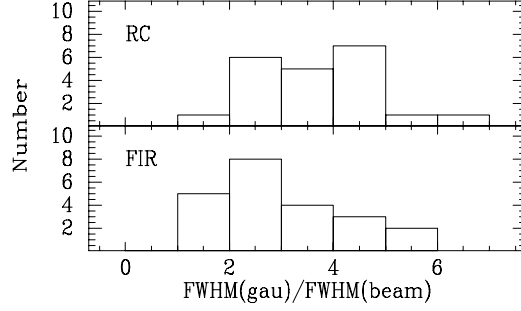


Fig. 5.— The full width at half maximum of the gaussian component is compared with that of the resolution beam. All the galaxies have the ratio greater than unity, implying that the gaussian component is not due to a compact unresolved source.

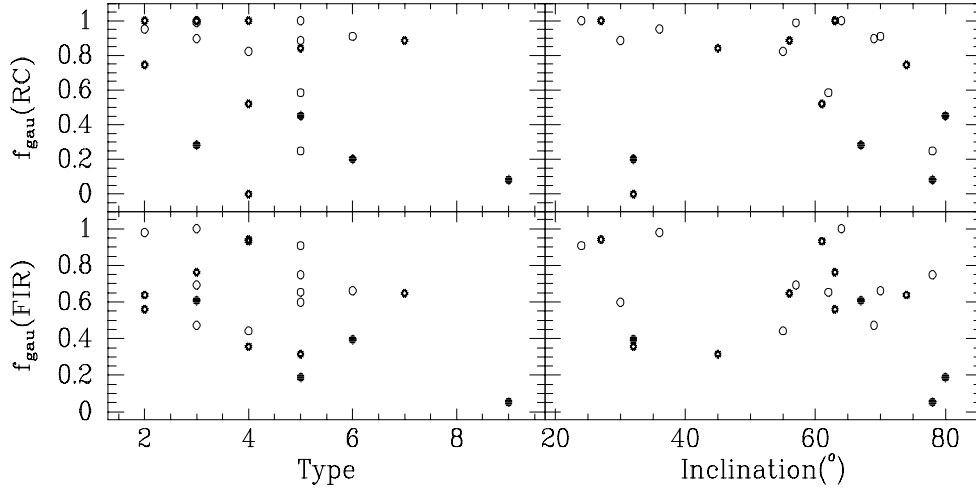


Fig. 6.— Flux fractions in the gaussian component ( $f_{\text{gau}}$ ) for the FIR and RC emissions are plotted against the Hubble type and inclination of the galaxies. Barred, un-barred and intermediate type galaxies are distinguished by the filled, open and starred circles respectively. Though a clear trend is missing in any of these plots, the lower envelope seems to decrease as Hubble type increases. The late-type galaxy NGC 4656 has the least  $f_{\text{gau}}$ .

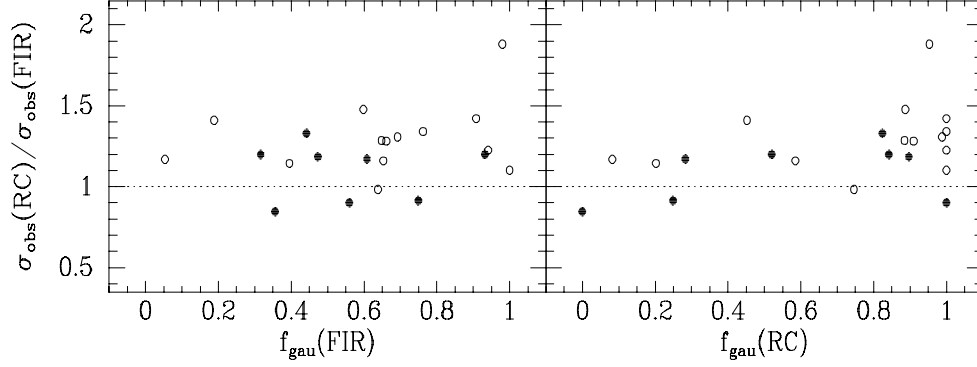


Fig. 7.— The ratio of the scale lengths of RC and FIR emission is plotted against the relative flux in the gaussian component ( $f_{\text{gau}}$ ).  $f_{\text{gau}}$  for the FIR and RC emission is shown separately in the two panels. In a given galaxy  $f_{\text{gau}}$  for FIR and RC deviates by more than 30% in eight galaxies which are identified by filled circles. Except in four galaxies (NGC 3628, 4192, 4321 and 4569), the RC scale lengths are larger than the FIR scale lengths.

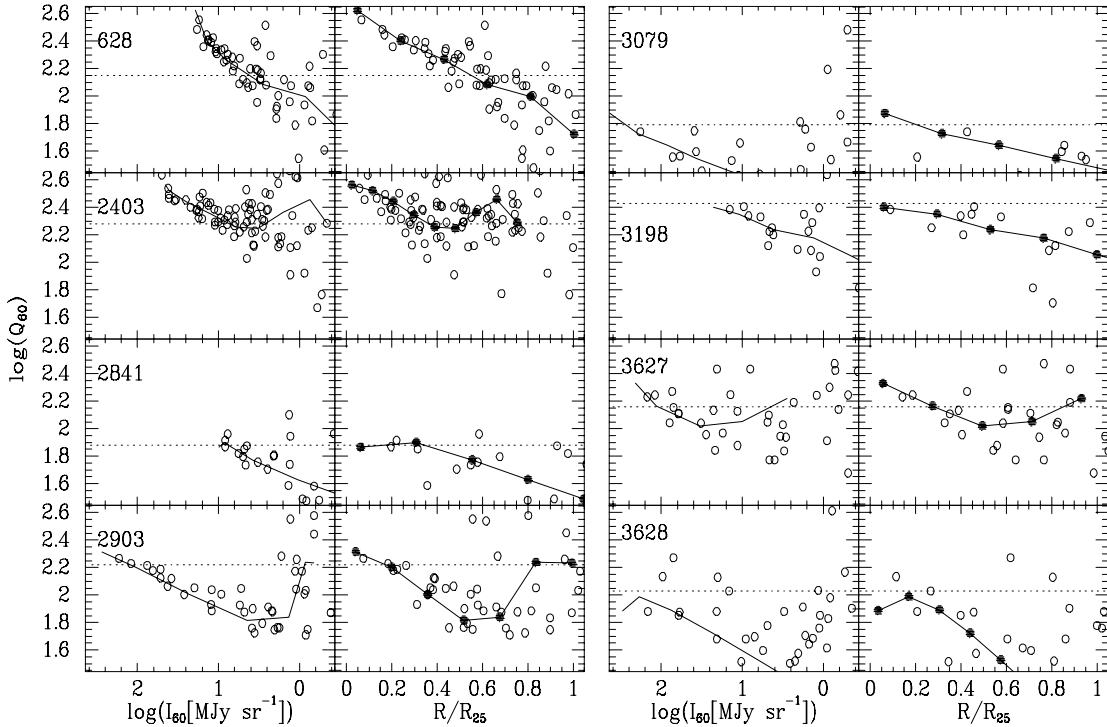


Fig. 8.—  $Q_{60}$  values within individual galaxies are plotted against the  $60\mu\text{m}$  intensity and the radial distance from the center. Open circles correspond to averages over  $1'$  pixels in galaxies. Results from azimuthally averaged radial profiles are shown by the thin line (left panel) and thick lines (right panel). The radial profiles are sampled at  $1'$  intervals, which are indicated by the solid dots on the right panel. In general  $Q_{60}$  values show a tendency to decrease by about factors 2–3 within half the optical radius of the galaxy.

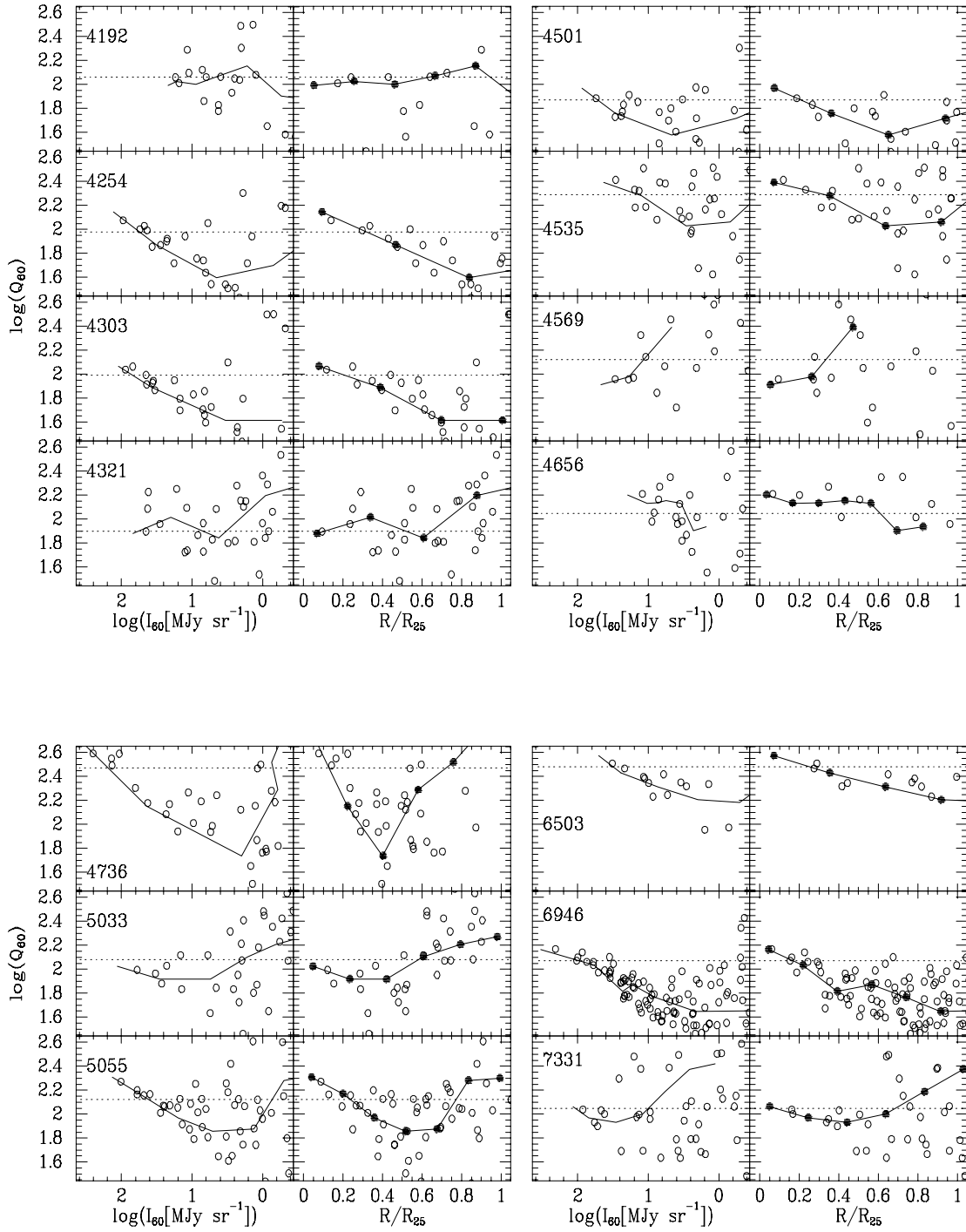


Fig. 8.— Continued.

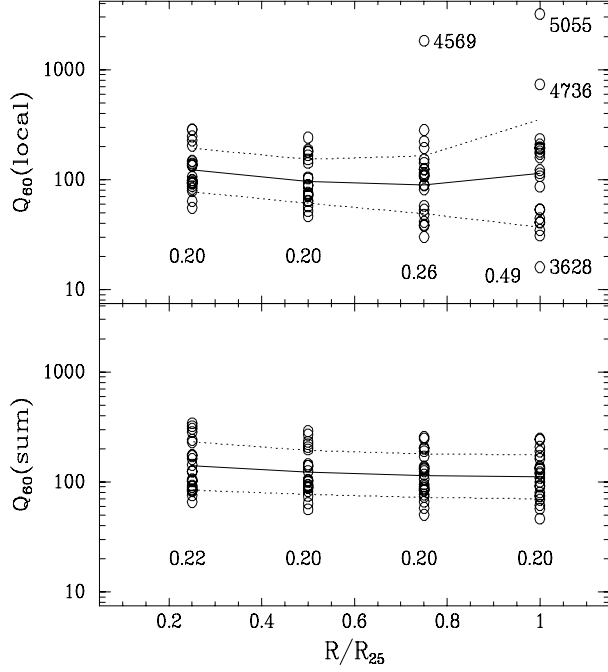


Fig. 9.—  $Q_{60}$  values for the program galaxies are plotted at 25, 50, 75 and 100% of the disk radius (top panel). Mean values at each of these radii are connected by a solid line. Dotted lines trace locations of 1-rms deviation from the mean. The values of the rms deviation (in log units) at the four radial distances as well as the NGC numbers of galaxies with maximum dispersion are noted. The bottom panel is similar to the top panel except that the plotted  $Q_{60}$  values are the result of integrating the fluxes inside successively larger radial zones. Hence the values at the outer-most position correspond to the global  $Q_{60}$  and dispersion.

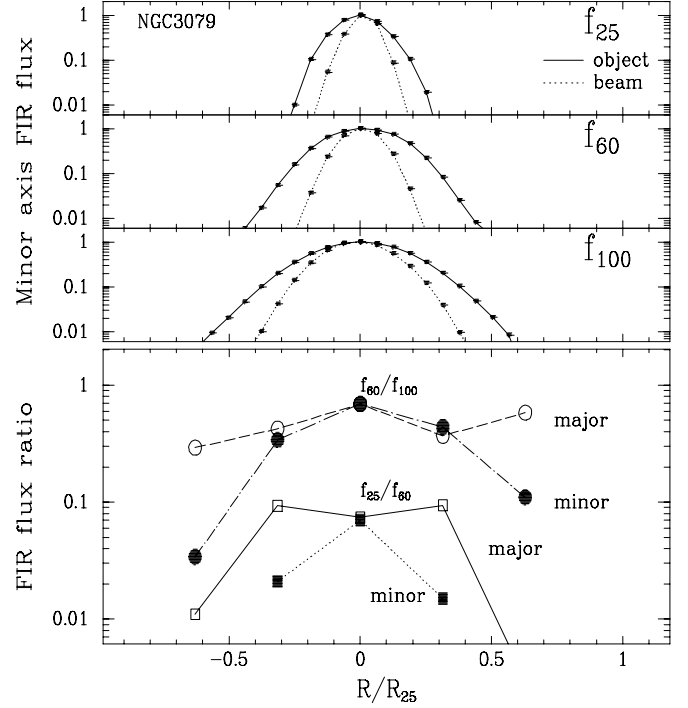


Fig. 10.— The FIR flux ratios (which are indicators of dust temperature) in 25, 60 and 100  $\mu\text{m}$  bands are plotted, in the bottom-most panel. The flux and beam profiles along the minor axis are plotted in the first three panels. The negative x-axis corresponds to the south-east side (see Fig. 1). Symbols denote the measured values, which are averages over 1 arcmin pixels. The connecting lines illustrate the steeper gradient along the minor axis, especially for the hotter dust ( $f_{25}/f_{60}$ ).